Chapter 5

MOTOR-DRIVEN MICROTUBULE DIFFUSION IN A PHOTOBLEACHED DYNAMICAL COORDINATE SYSTEM

In this collaborative project led by Soichi Hirokawa, I analyzed data and provided reagents. Specifically, I developed an image processing pipeline allowing me to analyze the speed of motor proteins based on microtubule gliding data. Additionally, I purified proteins and prepared buffers used in these experiments. This study is published and can be found with the following citation:

Soichi Hirokawa, Heun Jin Lee, Rachel A. Banks, Ana Isabel Duarte, Bibi Najma, Matt Thomson, and Rob Phillips. "Motor-driven microtubule diffusion in a photobleached dynamical coordinate system." In: *Proceedings of the National Academy of Sciences* 122.24 (2025), e2417020122. doi: 10.1073/pnas. 2417020122

Significance Statement: Individuals of active matter systems work together to generate large scale, ordered structures. However, the detailed dynamics occurring in the network bulk during this organization process are largely unknown. By photobleaching an actively contracting microtubule network, we show that filaments exhibit a local diffusion-like reorganization amid a global contraction at uniform rate, both of which can be tuned by the effective motor speed. Tuning these parameters alters the active contraction rates and effective diffusion constants, but maintains a conserved proportionality between the two. We thus find that motors play a dual role in the global contraction and local diffusive-like spread of the network.

5.1 Abstract

A hallmark feature of active matter systems is the ability of individual elements to interact and organize over length scales exceeding that of the constituent molecular players. However, the nature of internal redistribution that occurs in the bulk of the collective is less clear. Using light-dimerizable kinesin motors to spatially control the formation and contraction of a microtubule network, we deliberately photobleach a grid pattern onto the filament network serving as a transient and dynamic coordinate system to observe the deformation and translation of the remaining fluorescent squares of microtubules. We find that the network contracts at a rate set by

motor speed but is accompanied by a diffusive-like spread throughout the bulk of the contracting network with effective diffusion constant two orders of magnitude lower than that for freely-diffusing microtubules. We further find that on micron scales, the diffusive timescale is only a factor of ≈ 3 slower than that of advection regardless of conditions, showing that the global contraction and long-time relaxation from this diffusive behavior are both motor-driven but exhibit local competition within the network bulk.

Whether for schools of fish evading a sea lion or in the ordered array of microtubules comprising the spindle of dividing cells, coordinated movement and emergent patterning is a hallmark of biological dynamics across all biological scales. Curiosity surrounding the underlying principles dictating such a ubiquitous feature in biology have led to an explosion of theoretical [1, 2, 3, 4] and experimental efforts [5, 6, 7, 8, 9] to understand them. *In vitro* active matter systems offer a powerful means to study how cytoskeletal elements self-organize to generate a diverse array of networked structures. By mixing multimerized motors with filaments, a broad range of ordered patterns have been demonstrated, occurring in solutions which are spatially-homogeneous [5, 10, 9] or are locally defined through patterned light [11, 12, 13, 14]. A common observation from these assays is that the constitutive filaments rearrange in time under dynamics that appear to be primarily advective in nature. Recent efforts have led to several quantitative models that macroscopically describe the flow-like redistribution of microtubules under a range of conditions related to properties of the motors and filaments [15, 16, 17, 18, 19]. In addition to advective behavior, previous theoretical studies of contractile active gels have also shown that local fluctuations within a globally contracting network can give rise to a motor-driven diffusive-like effect among filaments [20, 21], a phenomenon that has been observed experimentally [22]. This seeming competition between active diffusion and advection invites a rigorous approach to distinguish these two effects.

In the work presented here, we incorporate fluorescence recovery after photobleaching (FRAP) into a light-controllable kinesin motor dimerization system [12, 23, 24] to characterize the interplay of motor-driven advective and diffusive dynamics. FRAP studies have typically been accompanied by various theory-based extensions of the diffusion equation to account for convective flow, reaction of molecules, or transport [25, 16, 26, 27, 28] and have been effectively applied to active *in vitro* systems to determine how filaments are redistributing into or elastically contracting

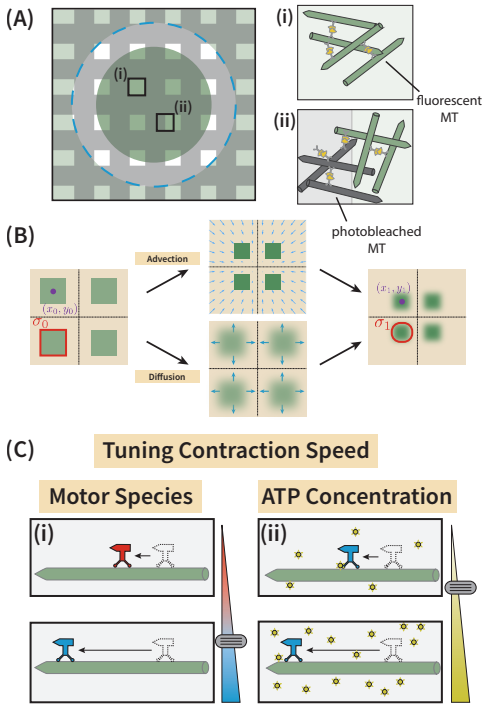

Figure 5.1: **FRAP-based approaches to studying advective and diffusive redistribution of cytoskeletal elements.** (A) Photobleaching a grid-like pattern leaves (i) squares of fluorescent microtubules (green) surrounded by (ii) non-fluorescent filaments (black) and allows us to examine the role of diffusive-like microtubule spread in the bulk of a global radially contracting network. Dashed blue circle outlines the edge of the dimerizing light inside of which the filaments couple and create a net contraction. (B) Tracking of centroids $[(x_0, y_0)$ to $(x_1, y_1)]$ and areas (σ_0 to σ_1) of the fluorescent squares allows us to quantify the advective and diffusive contributions in the contracting system. (C) The rates of these dynamics can be tuned by changing the effective motor speed through either (i) changes in the motor species or (ii) changes to the ATP concentration in the system. We tune these parameters to examine rates of contraction and bulk reorganization of microtubules in the contracting cytoskeletal network.

relative to the photobleached region [21, 29, 30, 31]. For our study, we photobleach a grid pattern onto a contracting microtubule network, which creates square fluorescent regions (Fig. 5.1(A)). By tracking the area and centroids of these regions, we are able to account for the advective contraction of the network. By measuring how the darkened photobleached lines blur, we can account for how much the microtubules in the network undergo diffusive behavior (Fig. 5.1(B)).

We find the choice of motor species [32] or the availability of ATP [33] are key parameters controlling the network dynamics (Fig. 5.1(C)). For example, by reduc-

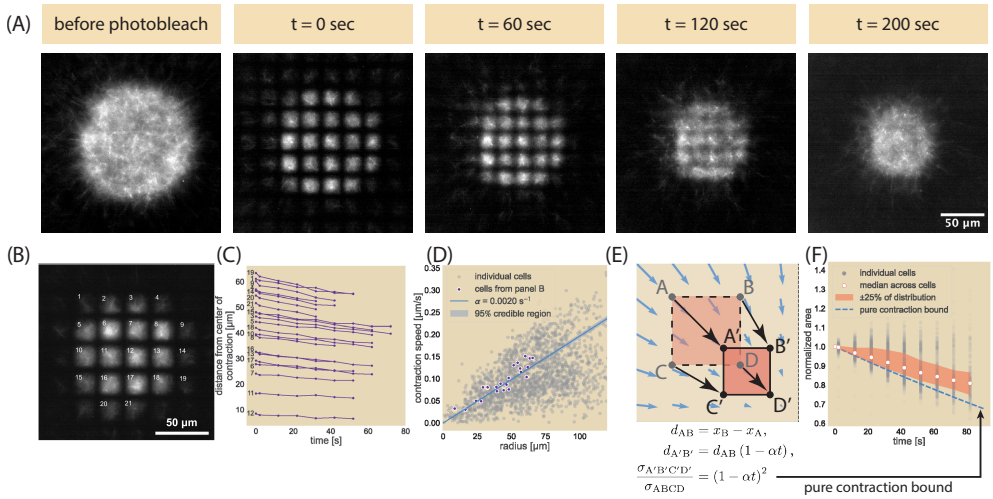

Figure 5.2: **Photobleaching a grid pattern onto the contracting microtubule network.** (A) Example dataset, where the microtubule field is photobleached and the deformations of the fluorescent regions observed using Ncd236 and 1.4 mM ATP. (B) Enumeration of individual fluorescent unit cells to (C) compute the distance of their centroids from the center of the network over time. Numbers correspond to labels from panel (B). (D) Plot of unit cell contraction speed as a function of their average distances from the center of the network, obtained by fitting the distance vs time data found in (C) to individual lines. The median contraction rate is $\alpha = 2.0 \times 10^{-3}$ s^{-1}. (E) Schematic of the unit cell deformation and expected area change under pure contraction. (F) The area of each unit cell is normalized against their initial area as obtained by the unit cell segmentation scheme and plotted as a function of time. The median normalized area is plotted in white among individual unit cells (gray). The red shaded region encompass points between the first and third quartiles of the distribution of all cells. Dashed blue line corresponds with the normalized area computed in (E) and using the median contraction rate obtained in (D).

ing motor speed, whether through decreased ATP concentration or slower motor species, the network globally contracts at a slower rate while the bulk of the network exhibits a decrease in effective diffusion constant. We further show that contraction rate and effective diffusion constant are linearly proportional measures across all of our conditions and give rise to a tightly bounded Peclét number slightly greater than one over micron length scales. While motors were understood to set the global contraction of the network, they play a second competing role within the network boundary that gives rise to a long-time relaxation on the local cytoskeletal structure.

5.2 Results

Photobleaching a grid pattern

To study the local redistribution of microtubules as the network contracts, we designed an augmented optical system that induces dimerization of kinesin through the iLid-micro system [34] in a circular region of radius 125 µm and images the microtubules [12, 24]. This modification includes a photobleaching element that allows us to photobleach a grid-like pattern into the microtubule channel at any point during contraction process (see Materials & Methods section and SI Sec S1.6). The end result is an array of squares roughly 12 µm in side length and 25 µm in center-to-center distance, much longer than the median microtubule length of $\approx$ 1.5 µm (see SI Sec S2). Fig. 5.2(A) shows an example of a grid pattern photobleached onto a microtubule network at different time points in its life history and the subsequent deformations of the bleached lines and fluorescent squares. As the image for the t = 0 sec timepoint in Fig. 5.2(A) shows, upon photobleaching the grid pattern, individual fluorescent squares, which we will call unit cells, are produced. Over a minute after photobleaching, unit cells contract toward the center of the network while the photobleached lines appear to blur away. By two minutes after photobleaching, neighboring unit cells appear to blend into each other and at later times any remnants of the photobleached pattern disappear.

Tracking fluorescent squares shows global contraction and local diffusive spread

To better quantify and understand the global network contraction dynamics, we segmented individual unit cells and measured their centroids and areas over successive frames (see SI Sec S3 and S4 for analysis). By tracking individual unit cells such as those shown in Fig. 5.2(B) and computing their distance from the center of the network over successive frames (Fig. 5.2(C)), we can determine the local contraction speeds, where we see a rough linear correspondence between distance and time. This was performed over many replicates and at different times in the contraction process (see SI Sec S5 for examples), all while maintaining the same initial size of the activation region (125 µm). We computed the slopes of each unit cell trajectory and compared the resultant speeds as a function of their distance from the network center (Fig. 5.2(D)) to find that the median contraction speed linearly increases with distance from the center, indicating a general uniform contraction rate of the entire microtubule network. We thus fit the velocity against the radius **r** with a line passing

through the origin (see SI Sec S6.1), giving the expression

$$\mathbf{v}(\mathbf{r}) = -\alpha \mathbf{r}, \tag{5.1}$$

where α is the contraction rate and thus measure a contraction rate and 95% credible region of $\alpha = 2.0 \times 10^{-3} \pm 5 \times 10^{-5}$ s^{-1}. Data separated by experimental replicates are available in SI Sec S7.

Despite the linear global contraction observed for the centroids, a more careful examination of the unit cells reveals that the network does not simply undergo purely elastic contraction. Suppose we took two points with different x-positions but the same y-position (x_A, y_A) and (x_B, y_A), respectively, such as points A and B in Fig. 5.2(E) that they have a distance d_0 of

$$d_0 = x_B - x_A, \tag{5.2}$$

where we will take $x_B > x_A$. If the two points were strictly subject to move from the velocity field given by Eq. 5.1, after time t their positions will have changed such that their distance d_1 is now

$$d_1 = \sqrt{[(x_B - \alpha x_B t - x_A + \alpha x_A t)]^2 + (y_A - \alpha y_A t - y_A + \alpha y_A t)^2}, \tag{5.3}$$

$$= (x_B - x_A)\,(1 - \alpha t)\,, \tag{5.4}$$

$$= d_0\,(1 - \alpha t)\,. \tag{5.5}$$

So the two points move closer by a factor of $1 - \alpha t$ in that time. We can make a similar argument for two points vertically separated. If we imagine this for all four points that make up the corners of a unit cell (points ABDC transforming to A'B'D'C' in Fig. 5.2(E)) and look at the change in area, we would expect that under a purely contractile active system subject to the uniform contraction rate measured from tracking the unit cell centroids, the area $A(t)$ would change from its initial size A_0 by

$$A(t) = A_0\,(1 - \alpha t)^2\,. \tag{5.6}$$

See SI Sec S8 for a more complete derivation. Fig. 5.2(F) shows the normalized area of each unit cell as a function of time in gray against this pure contraction scaling given as a blue dashed line. The median normalized area is shown as a white circle with a red outline. As can be seen by comparison with the shaded red region (representing the 50 percent of all cells that fall between the first and third quartiles of the distribution of cell areas), the majority of the experimental observations

are above the pure contraction bound. With the area being greater than that for a purely contracting network, we conclude that despite the global contraction of the network, filaments can locally spread and reorganize in the bulk. This observation is further affirmed by the merging of originally distinct fluorescent squares in the 120-second time point of Fig. 5.2(A), where a purely contractile network would cause fluorescent squares to remain distinct.

The effective diffusion constant is roughly two orders of magnitude lower than free diffusion of a microtubule

Since a purely contractile description is insufficient to fully capture the observed dynamics, we generalize our treatment of this contractile effect while accounting for diffusion by using an advection-diffusion equation to model the time evolution of the tubulin concentration $c(\mathbf{r}, t)$. Such a model has a material flux $\mathbf{J}$ of the form

$$\mathbf{J} = -D\nabla c + \mathbf{v}(\mathbf{r})\, c, \tag{5.7}$$

where D is the effective diffusion constant and $\mathbf{v}(\mathbf{r})$ is the velocity profile of the advective flow as a function of distance from the center of contraction r. As motivated by results shown in Fig. 5.2, we use the velocity field given by Eq. 5.1 with α as the computed contraction rate as shown in Fig. 5.2(D). When inserted into Eq. 5.7 and combined with the continuity equation, the advection-diffusion equation takes the form

$$\frac{\partial c}{\partial t} = -\nabla \cdot \mathbf{J}, \tag{5.8}$$

$$\frac{\partial c}{\partial t} = D\nabla^2 c + \nabla \cdot (\alpha \mathbf{r} c)\,. \tag{5.9}$$

We perform a series of careful explorations of the model in SI Sec S9-S11 to better understand the time-evolution of the concentration profile subject to Eq. 5.9 and to validate the implementation of our finite element method (FEM) using COMSOL Multiphysics®. Ultimately, these exercises confirm the importance of using a grid-like photobleaching pattern rather than a circular pattern, the latter of which would have convoluted the contributions of the radially-directed contraction with the more-isotropic diffusive-like spread. After validating our initial simulation, we turn to the use of FEM simulations on Eq. 5.9 to model our experimental results. We perform an FEM simulation of an individual unit cell, where we fix the FEM contraction rate to the experimentally-measured mean rate and sweep across various diffusion constants (see SI Sec S12 for implementation of a single unit cell in

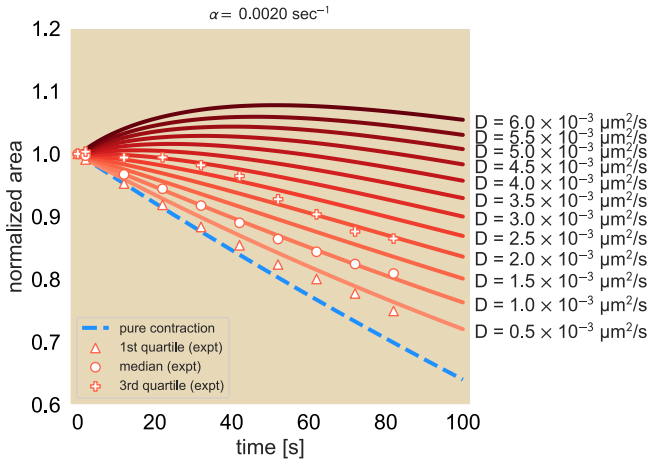

Figure 5.3: **Simulated concentration profiles for a linear advection-diffusion equation.** A family of curves for the expected normalized area of fluorescent squares subject to a fixed advection rate $\alpha = 2\times10^{-3}$ s^{-1} and varying diffusion constants. The 25th percentile (triangle), median (circle), and 75th percentile (plus sign) of the experimental area trajectories are overlaid onto the FEM results for comparison.

COMSOL). For example, for the Ncd236 motor at saturated levels of ATP, we show in Fig. 5.3 the family of normalized area trajectories for a single unit cell subject to the experimentally observed mean contraction rate of $\alpha = 2\times10^{-3}$ s^{-1}, and for diffusion constants D ranging from 5×10^{-4} to 6×10^{-3} $\frac{\mu m^2}{s}$. For comparison to the experimental data, we overlay the median (circle), the 1st quartile (triangle), and 3rd quartile (plus symbol) from the distribution of measured unit cell areas trajectories, where the quartiles give a sense of the trajectory variation. Here, we see that by minimizing least squares between the experiments and the simulation conditions, the median normalized area trajectory agrees best with the FEM trajectory with an effective diffusion constant of 1.0×10^{-3} $\frac{\mu m^2}{s}$. The first quartile of area trajectories from measurements lies between the pure contraction limit where $D_{\text{eff}} = 0$ and an effective diffusion constant $D_{\text{eff}} = 5.0 \times 10^{-4}$ $\frac{\mu m^2}{s}$. We interpret the first quartile results to mean the effective diffusion coefficient must be above 5.0×10^{-4} $\frac{\mu m^2}{s}$ in order to capture the majority of the data. The third quartile of area trajectories most closely follows the trajectory with an effective diffusion constant of $\approx 2.0 \times 10^{-3}$ $\frac{\mu m^2}{s}$ (see SI Sec S4.2 on fitting procedure), serving as a kind of upper bound. For context, the diffusion coefficients associated with the median and quartiles are all about two orders of magnitude smaller than the diffusion coefficient of a freely diffusing microtubule, which is ≈ 0.1 $\frac{\mu m^2}{s}$ (see SI Sec S2 for microtubule length;

equation for the longitudinal diffusion constant obtained from Ref [12]).

We also explored how well our FEM simulations could capture the qualitative features of the data set shown in Fig. 5.2(A), such as the merging of unit cells and the time scale of this process (see SI Sec S13). Our main finding from these efforts is, even for just qualitative comparisons, diffusion must be included in the theoretical description of the dynamics.

Changing effective motor speed proportionally changes contraction rate and effective diffusion constant

To test whether motors play a role in the diffusive-like effect, we next tuned the effective speed of the active elements, namely, the motors themselves. Two ways in which this can be done is by the choice of motor species or by changing the concentration of ATP. We chose optogenetic versions of previously characterized motor variants that span roughly an order of magnitude in speeds: Ncd236, Ncd281 [35], K401 expressed in bacteria [12], and K401 expressed in Sf9 cells [24] (See SI Sec S15 for Ncd281 construct designs and motor speeds and processivities). Fig. 5.4(A) shows the motors speeds for each of these motor types and the associated contraction rate. Interestingly, we observe a roughly linear relationship between contraction rate and motor speeds (see SI Sec S16.2). The effective diffusion coefficient also demonstrate a roughly linear trend (Fig. 5.4(B)). We note that even for the slowest motor Ncd281, a non-zero coefficient D_{eff} of 3×10^{-4} $\frac{\mu m^2}{s}$ is needed to recapitulate its corresponding unit cell area trajectories. This general tendency to increase the effective diffusion constant suggests that the motor speed may be responsible for the local microtubule effective diffusion.

We next examine how this local diffusive-like effect changes when we decrease the motor speed of a given species by reducing ATP concentrations. In order to traverse along microtubules, motors must hydrolyze ATP with each step they take. At saturated concentrations of ATP, motors can hydrolyze ATP at their maximal rate and therefore move at their maximum speed. At reduced ATP concentrations, the limited availability of ATP causes motors to hydrolyze ATP at a reduced rate, leading to an effective reduction in motor speed [36, 37, 38]. In the context of a contracting microtubule network, we hypothesize that this decrease in motor speed translates to a reduction in contraction rate, similar to the effect observed when using a slower motor species. We further hypothesize that for a constant motor concentration, reducing the concentration of ATP will increase the fraction of motors that do not

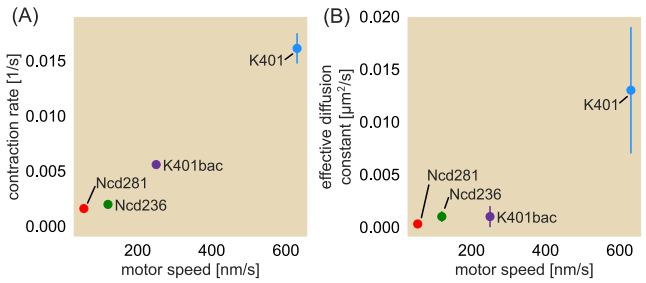

Figure 5.4: **Contraction rates and effective diffusion constants for four different motor types.** (A) Contraction rate as a function of motor speed. Here, the motors are (in order of motor speed as found in Table S2 of the SI Text) Ncd281 (red) [35], Ncd236 (green), K401 expressed in bacteria (purple), and K401 expressed in Sf9 cells (blue) [24]. (B) Corresponding effective diffusion constants as a function of motor speed where the circles denote the medians of the experimentally obtained normalized area trajectories and error bars denote the middle 50% of the distribution. Error bars for some data points are smaller than the radius for the size of the dots.

move along the microtubules and instead behave as passive crosslinkers, causing the areas of the fluorescent unit cells to fall closer to the pure contraction bound. To test this, we perform our photobleach experiment for Ncd236 and bacteria-expressed K401 at ATP concentrations spanning two orders of magnitude. We continue to use an ATP regeneration system so that the ADP concentration is negligible and therefore does not compete with ATP for the hydrolysis site [38] (see Materials and Methods). Fig. 5.5(A) and (C) show that for both Ncd236 (A) and K401 (C), as the concentration of ATP is decreased, the contraction rate of the network similarly decreases. At 25 μM ATP, the contraction rate with Ncd is roughly half of that at saturated levels. This concentration is also roughly the measured Michaelis constant of ATP hydrolysis by the motor [39]. However, at ATP concentrations below this Michaelis constant, we see that the network contraction, while still occurring for an ATP concentration of half the Michaelis constant for Ncd236, dramatically slows down. We fit the contraction rate against ATP concentration to the best fit of a Michelis-Menten equation to find that the expected Michaelis constant for ATP hydrolysis in the contracting network context (Ncd236: 30 ± 13 μM; bacterial-expressed K401: 47 ± 13 μM) is roughly the same as for measured motor speeds (Ncd236: ≈ 23 μM [39]; bacterial-expressed K401: 28.1 ± 0.9 μM [38]).

Decreasing the ATP concentration overall reduces the effective diffusion constant for Ncd236 (Fig. 5.5(B)). As the network dynamics scale with ATP concentration in a similar way to single-motor kinetics, our results show that motors are drivers of not

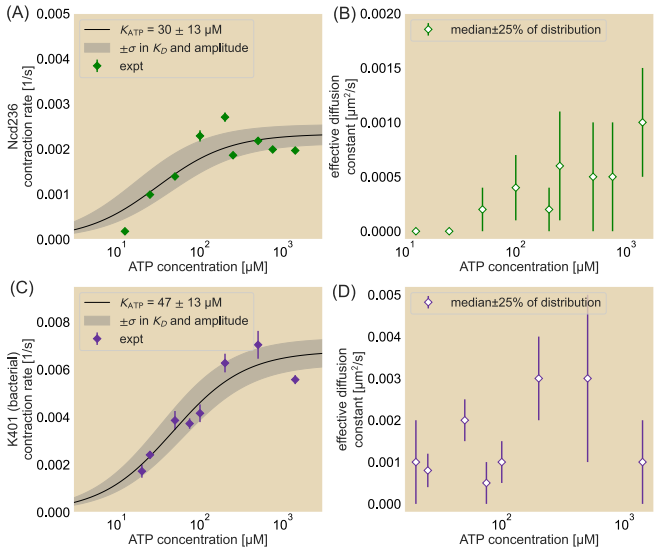

Figure 5.5: **Contraction rates and effective diffusion constants over a range of ATP concentrations.** Contraction rates (A and C) and effective diffusion constants (B and D) as a function of ATP concentration in the system. Motors used are Ncd236 (A and B) and K401 expressed in bacteria (C and D). Black line represents best fit to a Michaelis-Menten equation. Edges of the gray shaded region bounded to the left (right) using the Michaelis-Menten equation where the amplitude is the best fit plus (minus) one standard deviation and the Michaelis constant is the best fit minus (plus) one standard deviation. Effective diffusion constants fitted to the median area trajectories with error bars corresponding to fits spanning the middle 50% of the distribution motor types are presented.

only the contraction rate but also the local diffusion-like relaxation of the network. On the other hand, such a trend is less clear for bacteria-expressed K401 at some ATP concentrations (Fig. 5.5(D)). One possible explanation for the unclear trend is low motor processivity. If we consider the time a motor spends on a filament, we have $\langle \tau_{\text{on}} \rangle = k_{\text{off}}^{-1} = \frac{l \times p}{v_{\text{motor}}}$ for l the step size (8 nm), p the processivity, or the number of steps the motor takes before falling off, and v_{motor} the motor speed; in other words, the time that a microtubule is connected to the rest of the network is proportional to the processivity. This could mean that for motors of low processivity, there may be some mixing of passive diffusion and this active diffusion observed thus far. It is unclear to what extent the processivity of bacterial-expressed K401 differs from that of its Sf9-expressed variant and invites future examination to better understand the role of processivity on this diffusive-like effect. On the other hand, while Ncd236 is a non-processive motor, we suspect that cooperativity helps rescue a processive effect. It has been shown that cooperativity through multiple Ncds on

the same filament can recover a processivity similar to that of K401 [40], allowing Ncd236 to follow a general increase in effective diffusion with ATP concentration. However, the processivity of the bacterial-expressed K401 may differ from that of the highly-processive insect-expressed K401, which may play an additional role in the diffusive-like filament reorganization and making the relation between effective diffusion and ATP concentration less clear. This invites further exploration to resolve the underlying discrepancies.

Contraction rate and effective diffusion constant are unified in the Péclet number

From tuning the motor type and ATP concentration in our *in vitro* kinesin-microtubule system and measuring the resultant contraction and diffusion rates, we see when parameters increase the contraction rate of the network they also similarly increase the effective diffusion constant. This suggests a relationship between the advective and diffusive properties.

To characterize this, we make use of the Péclet number, a non-dimensional ratio

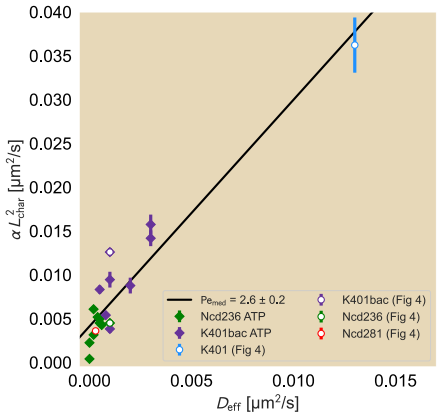

Figure 5.6: **Relation of contraction rate and effective diffusion constant**. Comparisons of contraction rate to effective diffusion constant are made for effective diffusion constants fitted to the median normalized area trajectories and obtained across all ATP concentration (diamonds) and motor species (hollow circles with colors matching those in Fig. 5.4) conditions. Contraction rates are multiplied by the square of a characteristic length scale, in this case roughly the median length of a microtubule in experiments (1.5 μm), to match the units of the effective diffusion constant. Slopes of lines are best fits of Pe, which are reported with their respective standard deviations in the legend.

between the rates of advection and diffusion in the system, given by

$$\mathrm{Pe} = \frac{\text{diffusive timescale}}{\text{advective timescale}}, \tag{5.10}$$

$$= \frac{L_{\mathrm{char}}^2/D}{L_{\mathrm{char}}/\mathrm{v}_{\mathrm{char}}}, \tag{5.11}$$

$$= \frac{\mathrm{v}_{\mathrm{char}} \times L_{\mathrm{char}}}{D}, \tag{5.12}$$

where L_{char} and $\mathrm{v}_{\mathrm{char}}$ are the characteristic length scale and characteristic advective velocity, respectively. L_{char} determines the length scale in the system over which the advective and diffusive timescales are compared. In our system, candidates for L_{char} may be as small as a typical microtubule in the assay and as large as the size of the contracting system. As the microtubule length is within an order of magnitude of the photobleached line and gives a sense of the local competition between diffusion and advection, we choose $L_{\mathrm{char}} = 1.5$ µm. We relate $\mathrm{v}_{\mathrm{char}}$ to L_{char} through the global contraction rate of the network α. In other words, $\mathrm{v}_{\mathrm{char}} = \alpha \times L_{\mathrm{char}}$. So we have

$$\mathrm{Pe} = \frac{\alpha\, L_{\mathrm{char}}^2}{D}. \tag{5.13}$$

To estimate the Péclet number, we plot the median contraction rates multiplied by the square of a characteristic length scale against the corresponding effective diffusion rates for all experimental conditions (ATP concentration as diamonds and motor species as hollow circles) in Fig. 5.6, which demonstrates a roughly linear relationship. The slope of the line gives Pe, specifically $\mathrm{Pe} = 2.6 \pm 0.2$. To get a sense for how much Pe varies due to variability within conditions, we find $\mathrm{Pe}_{25} = 4.5 \pm 0.5$ and $\mathrm{Pe}_{75} = 2.4 \pm 0.1$ for the first and third quartile datasets, respectively (see SI Sec S15), suggesting that Pe is tightly constrained. In all cases, $\mathrm{Pe} \gtrsim 1$, suggesting that the effect of diffusion is smaller than that of advection, but comparable to within an order of magnitude. This makes sense as the net effect of the unit cells, despite exhibiting a local diffusive-like effect, shrinks in area. Further, the rather narrow range in the Péclet number despite the spread in quartiles further suggests that the speed of the active elements sets both the global contraction of the network and the local spread of individual filaments. We recall that our choice of L_{char} allows us to examine the local competition between advection and diffusion. Had we chosen the side length of a unit cell or the size of the system as our size scale, we would see the increase in L_{char} results in $\mathrm{Pe} \gg 1$, demonstrating the greater dominance of the advective component over larger length scales, consistent with the net contraction in the network. Our results indicate that while advection generally dominates over

diffusion, most notably over longer length scales, the close linear relation between the two rates suggest that they are both set by the speed of the motors.

Interestingly, that a Péclet number relates the contraction rate and effective diffusion constant suggests a new interpretation of the advection-diffusion equation as written in Eq 5.9. Specifically, we can rework Eq 5.13, such that

$$D = \beta\alpha, \tag{5.14}$$

where $\beta \equiv \frac{L_{\text{char}}^2}{\text{Pe}}$. With this new relation, we next rewrite Eq 5.7 as

$$\mathbf{J} = -\underbrace{\alpha\,\mathbf{r}c}_{\text{advection}} - \underbrace{\alpha\,\beta\nabla c}_{\text{active diffusion}}, \tag{5.15}$$

such that Eq 5.9 now becomes

$$\frac{\partial c}{\partial t} = \alpha\nabla\cdot(\mathbf{r}c + \beta\nabla c)\,. \tag{5.16}$$

We emphasize again that β is dependent on quantities that are applied across all conditions namely, L_{char} and Pe, and thus is similarly fixed across the conditions examined here. Thus, if we used Pe_{med} we would obtain $\beta = 0.87\ \mu\text{m}^2$ as our value across conditions. Eq 5.16 creates a striking new viewpoint on the relation between the advective and diffusive terms. In particular, this equation tells us that there is only one parameter that varies across the conditions, namely the contraction rate α. Perhaps even more curious is the interpretation of the parameter β. Essentially, this factor tells us the coupling strength of the contraction rate on the diffusive effect in the system and suggests that tuning motor speed alone does not greatly alter this strength factor. We explore the connection between motor speed from our data and this new interpretation in Sec SI S16 as a call for further theoretical and experimental investigation of the fascinating coupling of active contraction and active diffusion. We note that a theory of the parameter β would need to account for how it depends upon motor processivity and stall force, for example.

5.3 Discussion

The dynamic cytoskeleton is critical to carrying out key processes within cells, such as the formation and maintenance of the mitotic spindle [41], cell division by cytokinesis [42], and as centers of morphogenetic information [43]. Such motor-filament structures are vital to a cell or organism, but how the constituent cytoskeletal elements reorganize to reach the same end configuration due to changes in biochemical

conditions has been unclear. In order to understand this response by the kinesin-microtubule network, we developed an experimental framework for probing the bulk redistribution of the filament network using a grid photobleaching pattern. By photobleaching the network, we observe that microtubules will undergo a diffusive-like spread that locally opposes the global, uniform contraction of the system. The diffusive-like behavior and contraction rate are jointly tuned by changes to the effective motor speed either from using different motor species or altering the ATP concentration. These effects also appear to occur from tuning crowding agents, a topic that we discuss in SI Sec S16-S17. In short, not only is the contraction an actively driven phenomenon, but so too is the diffusive-like behavior.

As we observed a general increase in effective diffusion constant with the increase in contraction rate, we further probed this relationship to find a roughly linear relationship between the two measurements. This suggests that the Péclet number, which is the ratio of the diffusive timescale to the advective one, remains roughly constant within the bulk of the contracting network regardless of the biochemical conditions we used here and further suggests that motor velocity not only sets the rate that the system contracts but also the effective diffusivity in the bulk.

Active diffusion has been observed in other active systems both *in vitro* [21, 29, 30, 31] and *in vivo* [44, 45, 46]. This phenomenon is particularly exciting in those cases where the diffusive-like motion exhibits a dependency on the availability of ATP. *In vitro*, a Michaelis-Menten like relationship has been observed between ATP concentration and the spatial rate of deformation of the system [30]. This relationship between the rate at which deformations occur and ATP concentration is consistent with our observations that both the macroscopic deformation rate and local diffusion are determined largely by an effective velocity of the motor. Furthermore, the fact that this ATP dependence also occurs in *in vivo* systems [45, 46] suggests interesting implications in the ability of cells to carry out key enzymatic reactions. One key parameter that has not yet been explored is the competition of ADP in the system. We recall that our work utilized an ATP recycling system that allowed us to ignore such competing effects. However, cells also have a supply of ADP that may compete with ATP for the ATP hydrolysis site of motors [38]. A natural extension of this study would involve systematically tuning the ratio of ATP to ADP to observe the effects of reorganization due to this competition and may provide key insights on the role of metabolic activity on altering the rates of ATP-dependent processes.

Various quantitative models have been made to recapitulate the experimentally ob-

served motor-filament dynamics [18, 11, 19, 21, 47, 23]. These models incorporate contractile stresses in the system, either through motor-driven activity or Stokeslets in the flow field, resulting in a net elastic behavior [11, 19, 23]. As we report here, a long-time relaxation term is required to create the diffusive-like filament redistribution in the network bulk. Recent treatments to introduce a long-time relaxation, as found in Ref [48], propose force-balance approaches that incorporate a viscoelastic stress to locally oppose the active stress underlying the elastic contraction. As our findings indicate that the relaxation is motor driven and transports filaments based on the direction of their orientation, we propose that an active viscoelastic-like stress term would be necessary and would need to depend on the motor speed and local polarity of the network. Indeed, other works account for the orientation $\vec{p}$ of the filaments not only for driving the movement of motors but as time-dependent variables through crosslink-generated torques [21, 47], offering encouraging pathways to recapitulate active cytoskeletal reorganization and necessitating measurements on local filament orientation.

Our work provides deeper insights into the extent of filament redistribution during network contraction, where the active element not only drives the global contractile behavior but also generates a local redistribution that can be tuned by their effective speeds. Our findings leave many unanswered and exciting questions about these self-organizing systems. Much is still not known about the origins of the network formation from the initially random orientation and uniform distribution of filaments prior to contraction. Specifically, the key criteria of the formed network, whether in the form of a density or order dependence, to drive the contraction process remain unclear. Photobleaching as applied in our work here provides a helpful macroscopic view of filament reorganization that can serve as a complement to other methods that are likely required to probe the dynamics of the filaments in the network, such as their orientation when they become coupled by the multimerized motors. Our work here offers new insights and a useful method for probing other key biochemical parameters of the cell such as different motor-microtubule ratios, admixtures of opposing motors, dynamic microtubules [49], more complex iLid-micro activation geometries [23], or with the introduction of ADP to compete against ATP-dependent reactions.

5.4 Materials and Methods

Microscopy set-up

The microscopy elements used to activate the iLid-micro dimerization and image the different fluorescence channels are similar to those found in Ross *et al.* [12]. Briefly, a digital light processing projector from Texas Instruments was used to activate the motor dimerization and image the microtubule channels. An excitation filter wheel was placed in front of the projector to filter out the different channels. Photobleaching was performed using a diode laser with a center wavelength of 642 nm. A piezoelectric mirror gimbal mount from Thorlabs was placed downstream of the laser to deflect the beam path over a small range before the laser light passes through a cylindrical lens array inserted into a direct-drive rotation mount. The gimbal mount can then sweep the projected lines laterally to thicken the photobleaching lines before the rotation mount is rotated 90° and the gimbal mount changes the deflecting angle of the beampath in the orthogonal direction. Imaging is performed using a 20x objective. More details are available in the SI Sec S1.6.

Microtubule network assay

The microtubule network formation and contraction assay is set up similarly as in Ross *et al.* [12]. Micro- and iLid-tagged motors are mixed in equal motor monomer ratios with GMPCPP-stabilized microtubules labeled with Alexa 647 in a reaction mix containing among other components ATP, ATP recycling reagents including pyruvate kinase and phosphoenolpyruvate (PEP), and pluronic as a crowding agent. While elements of the oxygen scavenging are kept in the reaction, the glucose oxidase is removed from the reaction to ensure photobleaching. Removal of these oxygen scavengers minimally affects fluorescence intensity during imaging from using the projector over the time range over which the data is analyzed, as shown in SI Sec S3.

Image acquisition arrangement

Control of the light-dimerizing activation, photobleach laser activation, and imaging are performed through the Micro-Manager (MM) software [50, 51] while photobleaching is synchronized using a series of in-house compiled executable files that control the movement of the gimbal and rotation mounts. During acquisition, a beanshell script in MM changes the projection pattern on the DLP to create a circular light pattern of radius 125 µm for the iLid activation and full field for the imaging channels. When the desired state of the microtubule network is reached for

performing photobleaching, the script completes the image acquisition cycle before turning on the photobleaching laser and calling to the executables to create the grid before the next acquisition cycle.

Motor purification

Kinesin motors are expressed using the pBiex-1 vector transfected in Sf9 suspension cells. Cells are transfected at 5-7 µg for every 15×10^6 cells at a starting concentration 10^6 cells per mL of Sf900-III media using a liposome-based transfection regent (Escort IV Transfection Reagent). Cells are harvested $\backsim$60-72 hours after transfection and purified using the FLAG affinity tag and anti-FLAG antibody resins. Proteins are stored in 50% glycerol by volume with 1.5 mM DTT, 50 µM EDTA, 50 µM EGTA, and 15 µM ATP and stored at -20°C. Full storage buffers and final concentrations of components are available in the SI.

Data Availability

All data and code are publicly available. Raw image files and COMSOL simulation file can be downloaded from the CaltechDATA research data repository under the DOI:10.22002/f23ds-f2v87. Analyzed data files and code generated by Python (for analyses) and BeanShell Scripts and C# (for hardware communication) for the work presented here are available on the dedicated GitHub repository under the DOI:10.5281/zenodo.12806576.

5.5 Acknowledgements

We thank members of the Rob Phillips lab for useful discussions. We would also like to thank the David Van Valen and Rebecca Voorhees labs for providing resources for performing the protein expression and purification. We also thank Justin Bois, Griffin Chure, Peter Foster, Sebastian Fürthauer, Victor Gomez, Stephan Grill, Catherine Ji, Frank Jülicher, Matthias Merkel, Daniel Needleman, Leïla Perié, Henk Postma, Madan Rao, Shahriar Shadkhoo, and Fan Yang. This work was supported by 1R35 GM118043 and 2R35 GM118043 Maximizing Investigators' Research Awards (MIRA) (to R.P.).

References

[1] Tamás Vicsek et al. "Novel type of phase transition in a system of self-driven particles." In: *Physical Review Letters* 75.6 (1995), pp. 1226–1229.

[2] John Toner and Yuhai Tu. “Long-range order in a two-dimensional dynamical *XY* model: how birds fly together.” In: *Physical Review Letters* 75.23 (1995), pp. 4326–4329.

[3] Sriram Ramaswamy. “The mechanics and statistics of active matter.” In: *Annual Review of Condensed Matter Physics* 1 (2010), pp. 323–345.

[4] Jonas Denk and Erwin Frey. “Pattern-induced local symmetry breaking in active-matter systems.” In: *Proceedings of the National Academy of Sciences of the United States of America* 117.50 (2020), pp. 31623–31630.

[5] François J. Nédélec et al. “Self-organization of microtubules and motors.” In: *Nature* 389.6648 (1997), pp. 305–308.

[6] Arshad Kudrolli et al. “Swarming and swirling in self-propelled polar granular rods.” In: *Physical Review Letters* 100.5 (2008), p. 058001.

[7] Nitin Kumar et al. “Flocking at a distance in active granular matter.” In: *Nature Communications* 5 (2014), p. 4688.

[8] Katherine Copenhagen et al. “Topological defects promote layer formation in *Myxococcus xanthus* colonies.” In: *Nature Physics* 17.2 (2021), pp. 211–215.

[9] Tim Sanchez et al. “Spontaneous motion in hierarchically assembled active matter.” In: *Nature* 491 (7424 2012), pp. 431–434.

[10] Thomas Surrey et al. “Physical properties determining self-organization of motors and microtubules.” In: *Science* 292.5519 (2001), pp. 1167–1171.

[11] Matthias Schuppler et al. “Boundaries steer the contraction of active gels.” In: *Nature Communications* 7.13120 (2016), pp. 1–10.

[12] Tyler D. Ross et al. “Controlling organization and forces in active matter through optically defined boundaries.” In: *Nature* 572 (2019), pp. 224–229.

[13] Rui Zhang et al. “Spatiotemporal control of liquid crystal structure and dynamics through active patterning.” In: *Nature Materials* 20.6 (2021), pp. 875–882.

[14] L M Lemma et al. “Spatio-temporal patterning of extensile active stresses in microtubule-based active fluids.” In: *PNAS Nexus* 2.5 (2023), pgad130.

[15] Ha Youn Lee and Mehran Kardar. “Macroscopic equations for pattern formation in mixtures of microtubules and molecular motors.” In: *Physical Review Letters E* 64.5 (2001), p. 056113.

[16] François Nédélec, Thomas Surrey, and A.C. Maggs. “Dynamic concentration of motors in microtubule arrays.” In: *Physical Review Letters* 86.14 (2001), pp. 3192–3195.

[17] Sumithra Sankararaman and Gautam I. Menon. “Self-organized pattern formation in motor-microtubule mixtures.” In: *Physical Review Letters E* 70.3 (2004), p. 031905.

[18] Julio M. Belmonte, Maria Leptin, and François Nédélec. “A theory that predicts behaviors of disordered cytoskeletal networks.” In: *Mol Syst Biol* 13.941 (2017), pp. 1–13.

[19] Peter J. Foster et al. “Active contraction of microtubule networks.” In: *eLife* 4.e10837 (2015), pp. 1–21.

[20] Fred C. MacKintosh and A. J. Levine. “Nonequilibrium mechanics and dynamics of motor-activated gels.” In: *Physical Review Letters* 100 (1 2008), p. 018104.

[21] Sebastian Fürthauer et al. “Self-straining of actively crosslinked microtubule networks.” In: *Nature Physics* 15 (2019), pp. 1295–1300.

[22] Igor M. Kulic et al. “The role of microtubule movement in bidirectional organelle transport.” In: *Proceedings of the National Academy of Sciences of the United States of America* 105.29 (2008), pp. 10011–10016.

[23] Zijie Qu et al. “Persistent fluid flows defined by active matter boundaries.” In: *Communications Physics* 4.198 (2021), pp. 1–9.

[24] Rachel A. Banks et al. “Motor processivity and speed determine structure and dynamics of motor-microtubule assemblies.” In: *eLife* 12 (2023), e79402.

[25] D Axelrod et al. “Mobility measurement by analysis of fluorescence photobleaching recovery kinetics.” In: *Biophysical Journal* 16.9 (1976), pp. 1055–1069.

[26] José Braga, James G. McNally, and Maria Carmo-Fonseca. “A reaction-diffusion model to study RNA motion by quantitative fluorescence recovery after photobleaching.” In: *Biophysical Journal* 92.8 (2007), pp. 2694–2703.

[27] Mohit Kumar, Mario S. Mommer, and Victor Sourjik. “Mobility of cytoplasmic, membrane, and DNA-binding proteins in *Escherichia* coli.” In: *Biophysical Journal* 98.4 (2010), pp. 552–559.

[28] Maria-Veronica Ciocanel et al. “Analysis of active transport by fluorescence recovery after photobleaching.” In: *Biophysical Journal* 112.8 (2017), pp. 1714–1725.

[29] Alexandra M. Tayar, Michael F. Hagan, and Zvonimir Dogic. “Active liquid crystals powered by force-sensing DNA-motor clusters.” In: *Proceedings of the National Academy of Sciences of the United States of America* 118.30 (2021), e210873118.

[30] Linnea M. Lemma et al. “Multiscale microtubule dynamics in active nematics.” In: *Physical Review Letters* 127.14 (2021), p. 148001.

[31] Alexandra Colin et al. “Friction patterns guide actin network contraction.” In: *Proceedings of the National Academy of Sciences of the United States of America* 120.39 (2023), e2300416120.

[32] Harukata Miki et al. “All kinesin superfamily protein, KIF, genes in mouse and human.” In: *Proceedings of the National Academy of Sciences of the United States of America* 98.13 (2001), pp. 7004–7011.

[33] Hideyuki Yaginuma et al. “Diversity in ATP concentrations in a single bacterial cell population revealed by quantitative single-cell imaging.” In: *Scientific Reports* 4.6522 (2014), pp. 1–7.

[34] Gurkan Guntas et al. “Engineering an improved light-induced dimer (iLID) for controlling the localization and activity of signaling proteins.” In: *Proceedings of the National Academy of Sciences of the United States of America* 112.1 (2015), pp. 112–117.

[35] Nicholas F. Endres et al. “A lever-arm rotation drives motility of the minus-end-directed kinesin Ncd.” In: *Nature* 439.7078 (2006), pp. 875–8.

[36] Jonathon Howard, A. J. Hudspeth, and Ronald D. Vale. “Movement of microtubules by single kinesin molecules.” In: *Nature* 342.6246 (1989), pp. 154–158.

[37] Koen Visscher, Mark J. Schnitzer, and Steven M Block. “Single kinesin molecules studied with a molecular force clamp.” In: *Nature* 400.6740 (1999), pp. 184–189.

[38] William R. Schief et al. “Inhibition of kinesin motility by ADP and phosphate supports a hand-over-hand mechanism.” In: *Proceedings of the National Academy of Sciences of the United States of America* 101.5 (2004), pp. 1183–1188.

[39] Kelly A. Foster, J. J. Correia, and Susan P. Gilbert. “Equilibrium binding studies of Non-claret disjunctional protein (Ncd) reveal cooperative interactions between the motor domains.” In: *Journal of Biological Chemistry* 273.52 (1998), pp. 35307–35318.

[40] Ken’ya Furuta et al. “Measuring collective transport by defined numbers of processive and nonprocessive kinesin motors.” In: *Proceedings of the National Academy of Sciences of the United States of America* 110.2 (2013), pp. 501–506.

[41] Christina L. Hueschen et al. “Microtubule end-clustering maintains a steady-state spindle shape.” In: *Current Biology* 29 (4 2019), 700–708.e5.

[42] Ann L. Miller. “The contractile ring.” In: *Current Biology* 21.24 (2012), R976–R978.

[43] Yonit Maroudas-Sacks et al. “Topological defects in the nematic order of actin fibres as organization centres of *H*ydra morphogenesis.” In: *Nature Physics* 17 (2021), pp. 251–259.

[44] Clifford P. Brangwynne, Fred C. MacKintosh, and David A. Weitz. "Force fluctuations and polymerization dynamics of intracellular microtubules." In: *Proceedings of the National Academy of Sciences of the United States of America* 104.41 (2007), pp. 16128–16133.

[45] Stephanie C. Weber, Andrew J. Spakowitz, and Julie A. Theriot. "Nonthermal ATP-dependent fluctuations contribute to the in vivo motion of chromosomal loci." In: *Proceedings of the National Academy of Sciences of the United States of America* 109.19 (2012), pp. 7338–7343.

[46] Ming Guo et al. "Probing the stochastic, motor-driven properties of the cytoplasm using force spectrum microscopy." In: *Cell* 158.4 (2014), pp. 822–832.

[47] Sebastian Fürthauer, Daniel J. Needleman, and Michael J. Shelley. "A design framework for actively crosslinked filament networks." In: *New Journal of Physics* 23.1 (2021), p. 013012.

[48] Fan Yang et al. "Dynamic flow control through active-matter programming language." In: *arXiv* (2022), pp. 1–9. DOI: https://doi.org/10.48550/arXiv.2208.12839.

[49] William G. Hirst et al. "Differences in Intrinsic Tubulin Dynamic Properties Contribute to Spindle Length Control in Xenopus Species." In: *Current Biology* 30.11 (2020), pp. 2184–2090.

[50] Arthur D. Edelstein et al. "Computer control of microscopes using μManager." In: *Current Protocols in Molecular Biology* (2010), pp. 14.20.1–14.20.17.

[51] Arthur D. Edelstein et al. "Advanced methods of microscope control using μManager software." In: *Journal of Biological Methods* 1.2 (2014), e11. DOI: doi:10.14440/jbm.2014.36.